ROYAL SOCIETY OPEN SCIENCE

royalsocietypublishing.org/journal/rsos

Research

Cite this article: Schindler DJ, Clarke J, Barahona M. 2023 Multiscale mobility patterns and the restriction of human movement. *R. Soc. Open Sci.* **10**: 230405.
https://doi.org/10.1098/rsos.230405

Received: 11 April 2023
Accepted: 18 September 2023

Subject Category:
Mathematics

Subject Areas:
applied mathematics

Keywords:
network analysis, computational social science, scales of human mobility, COVID-19 lockdown, multiscale community detection

Author for correspondence:
Mauricio Barahona
e-mail: m.barahona@imperial.ac.uk

Electronic supplementary material is available online at https://doi.org/10.6084/m9.figshare.c.6858353.

THE ROYAL SOCIETY PUBLISHING

Multiscale mobility patterns and the restriction of human movement

Dominik J. Schindler, Jonathan Clarke and Mauricio Barahona

Department of Mathematics, Imperial College London, London SW7 2BX, UK

DJS, 0000-0002-8728-9286; JC, 0000-0003-1495-7746; MB, 0000-0002-1089-5675

From the perspective of human mobility, the COVID-19 pandemic constituted a natural experiment of enormous reach in space and time. Here, we analyse the inherent multiple scales of human mobility using Facebook Movement maps collected before and during the first UK lockdown. Firstly, we obtain the pre-lockdown UK mobility graph and employ multiscale community detection to extract, in an unsupervised manner, a set of robust partitions into flow communities at different levels of coarseness. The partitions so obtained capture intrinsic mobility scales with better coverage than nomenclature of territorial units for statistics (NUTS) regions, which suffer from mismatches between human mobility and administrative divisions. Furthermore, the flow communities in the fine-scale partition not only match well the UK travel to work areas but also capture mobility patterns beyond commuting to work. We also examine the evolution of mobility under lockdown and show that mobility first reverted towards fine-scale flow communities already found in the pre-lockdown data, and then expanded back towards coarser flow communities as restrictions were lifted. The improved coverage induced by lockdown is well captured by a linear decay shock model, which allows us to quantify regional differences in both the strength of the effect and the recovery time from the lockdown shock.

1. Introduction

Spatiotemporal patterns of population mobility reveal important aspects of human geography, such as social and economic activity [1], the evolution of cities and economic areas [2], the response to natural disasters [3] or the spread of human infectious diseases [4]. Whilst mobility patterns are linked to, and influenced by, both geographical and administrative boundaries [5], they are also a direct reflection of social behaviour and thus

provide additional insights into the natural evolution of socio-economic interactions at the population level. The increasing access to detailed and continuously updated mobility datasets from various sources (e.g. mobile devices [5], GPS location traces [6], Twitter data [3]) opens up the opportunity to develop further quantitative approaches to harness the richness of such data [7–9].

Access to mobility data has recently become more widespread due to the COVID-19 pandemic, which prompted governments across the world to impose a range of restrictions on the daily activities and movements of their citizens [10]. Such mobility data were of immediate use to refine and assess interventions targeting the spread of COVID-19 [11–15] and to evaluate the unequal effects of the pandemic across populations [12]. Yet, from the perspective of mobility, the pandemic also constituted a natural experiment of enormous reach in space and time that accelerated both the sharing of such datasets and the study of a severe mobility shock, in which human activities were curtailed to reduced areas for a sustained period [16–21].

An important aspect of mobility is the presence of inherent spatial and temporal scales as a result of e.g. administrative divisions, patterns of social interactions, jobs and occupations, as well as diverse means of transportation [1]. Recent work [6,22] has shown that this multiscale, nested structure of human activities contributes to the scale-free behaviour that had been previously found empirically [7,8,23].

Here, we apply data-driven, unsupervised network methods to study the multiscale structure of UK mobility in data collected before and during the first COVID-19 lockdown. Data from user-enabled, anonymized 'Facebook Movement maps' between UK locations [24] are used to construct directed, weighted mobility graphs which are then analysed using unsupervised multiscale community detection [25–28] to extract inherent flow communities at different levels of coarseness. Hence, the inherent mobility scales emerge directly as robust flow communities in the data, obtained here through a scale selection algorithm.

Our results show that multiscale flow communities extracted from the baseline, pre-lockdown data broadly agree with the hierarchy of nomenclature of territorial units for statistics (NUTS) administrative regions, yet with distinctive features that result from commuting patterns cutting across administrative divisions. In addition, the flow communities at the fine scale not only match well travel to work areas (TTWAs) [29], a geography of local labour markets computed by the UK Office for National Statistics from 2011 Census data on residency and place of work for workers older than 16 years, but also capture human mobility patterns beyond commuting to work. We then quantify the extent to which mobility patterns under lockdown conform to the flow communities found in pre-lockdown data using data collected during the first UK COVID-19 lockdown (March–June 2020). We find that the imposition of lockdown reverted mobility towards the local, fine-scale pre-lockdown flow communities, and as restrictions were lifted, mobility patterns expanded back towards the coarser pre-lockdown flow communities, thus providing empirical evidence for the presence of a quasi-hierarchical intrinsic organization of human mobility at different scales [6]. Finally, we find regional differences in the response to the lockdown, in both the strength of the mobility contraction and the time scale of recovery towards pre-lockdown mobility levels.

2. Results

We use mobility data provided by Facebook under the 'Data for Good' programme [24] to construct directed, weighted networks of human mobility in the UK. The anonymized datasets ('Facebook Movement maps' [24,30]), which are collected from user-enabled location tracking, quantify frequency of movement of individuals between locations over time, thus capturing temporal changes in population mobility before and during the COVID-19 pandemic [18,19]. For details of the network construction, see §4.1.

Our data cover mobility patterns in all four nations of the UK before, during and after the first nationwide COVID-19 lockdown, which was imposed on 24 March 2020 (see below for more details). In the following, we first analyse the pre-lockdown baseline mobility, from which we obtain intrinsic partitions at different scales and then explore how the changes after lockdown mobility restrictions were imposed map onto those baseline scales.

2.1. The directed graph of baseline UK mobility: quasi-reversibility and commuting travel patterns

By using pre-lockdown mobility data (average of 45 days before 10 March 2020), we construct a strongly connected directed graph G with weighted adjacency matrix $A \neq A^T$ (figure 1*a*). The $N = 3125$ nodes of this

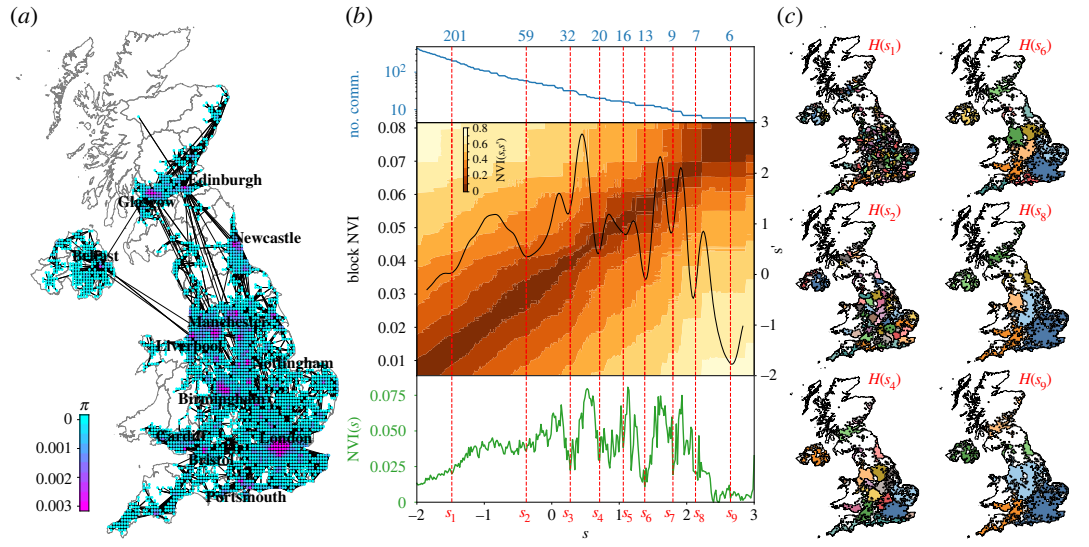

Figure 1. Multiscale structure in the baseline mobility network. (*a*) Using mobility data averaged over 45 days before 10 March 2020, we create a weighted directed graph ($N = 3125$ nodes, $E = 34\,224$ edges) with edge weights equal to the average daily number of trips between geographic tiles (nodes). The stationary distribution π (equation (2.3)) of the associated random walk indicates high centrality of urban areas. (*b*) Multiscale community detection on the baseline mobility network using Markov stability (MS) analysis. We find optimized MS partitions that are robust both across scales (blocks of low normalized variation of information, NVI(s, s')) and within scale (dips in NVI(s)). To find robust optimal partitions, we first determine basins in Block NVI(s) (the pooled diagonal of NVI(s, s')) and then find the minima of NVI(s) for each basin (see §4.2). This selection process leads to nine robust scales (s_1, …, s_9), from finer to coarser. (*c*) The graph partitions for the six scales with the lowest Block NVI are plotted on the UK map, with different colours indicating different communities.

graph correspond to geographic tiles (width between 4.8 and 6.1 km, see electronic supplementary material, figure S1*a*), and the directed edges have weights A_{ij} corresponding to the average daily number of inter-tile trips from tile i to j (see §4.1 for the notion of 'trip' within the Facebook dataset, and some of its caveats). The total average number of daily inter-tile trips is 2 475 527, compared with 10 416 968 intra-tile trips. The matrix A is very sparse, with 99.7% of its entries equal to zero, i.e. there are no direct trips registered between the overwhelming majority of tile pairs. Furthermore, the non-zero edge weights are highly heterogeneous, ranging from 1.4 to 6709 daily trips (average 72.3, coefficient of variation 2.8), underscoring the large variability in trip frequency across the UK.

To assess the directionality of the baseline network, we first compute the pairwise relative asymmetry (PRA) for each pair of tiles ij,

$$0 \leq \mathrm{PRA}_{ij} := \frac{|A_{ij} - A_{ji}|}{A_{ij} + A_{ji}} \leq 1, \tag{2.1}$$

defined for pairs where $A_{ij} + A_{ji} > 0$. The distribution of the PRA_{ij} (electronic supplementary material, figure S3) shows that 25% of the tile pairs have $\mathrm{PRA} \geq 0.23$, a substantial asymmetry, including 3226 one-way connections (8.64% of the total) with $\mathrm{PRA} = 1$. It is thus helpful to use network analysis tools that can deal with directed graphs [31].

A natural strategy for the analysis of directed graphs is to employ a diffusive process on the graph to reveal important properties of the network, such as node centrality [32,33] or graph substructures [27], while respecting edge directionality. We consider a discrete-time random walk on graph G defined in terms of the $N \times N$ transition probability matrix M:

$$M := D_{\mathrm{out}}^{+} A, \tag{2.2}$$

where D_{out}^{+} is the pseudo-inverse of $D_{\mathrm{out}} = \mathrm{diag}(\mathbf{d}_{\mathrm{out}})$, the diagonal matrix of out-strengths $\mathbf{d}_{\mathrm{out}} = A\,\mathbf{1}_N$. A key property of the random walk is its stationary distribution $\boldsymbol{\pi}$, a $1 \times N$ node vector defined through the equation

$$\boldsymbol{\pi} = \boldsymbol{\pi} M. \tag{2.3}$$

The component π_i is a measure of centrality (or importance) of node i; a high value of π_i means that the random walk on G is expected to visit node i often at stationarity [34]. This is equivalent to PageRank

without teleportation [35]. As expected, the centralities π_i are highly correlated ($R^2 = 0.97$) with another node centrality measure, the out-strengths $d_{\text{out},i}$. Interestingly, the centralities π_i are also correlated with the intra-tile mobility ($R^2 = 0.83$), a measure that is not used in the computation of $\boldsymbol{\pi}$ (see electronic supplementary material, figure S2 for details). Therefore, urban areas display high centrality due to the concentration of human mobility in those areas (figure 1*a*).

A random walk on a directed graph might still not display strong directionality at equilibrium. This is our finding here: the random walk defined by M fulfils approximately the detailed balance condition,

$$\Pi M \simeq \Pi M^T \quad \text{with} \quad \frac{\|\Pi M - \Pi M^T\|_F}{\|\Pi M\|_F} = 0.033,$$

where $\Pi = \text{diag}(\boldsymbol{\pi})$ and $\|\cdot\|_F$ denotes the Frobenius norm (see electronic supplementary material, figure S3 and [27,36] for a more in-depth discussion). The random walk for our mobility graph is therefore close to being time reversible at equilibrium [34], so that the probability of following a particular trajectory from node i to j is almost equal to the probability of going back on the same trajectory from j to i. This property coincides with our intuition that most journeys in the mobility network are linked to commuting travel patterns.

2.2. Unsupervised community detection reveals intrinsic multiscale structure in the baseline mobility data

To extract the inherent scales in the UK mobility data, we apply multiscale community detection to the baseline directed network. We use Markov stability (MS) [25], a methodology that reveals intrinsic, robust graph partitions across all scales through a random walk Laplacian that simulates individual travel on the network based on the observed average daily trips. As random walkers explore the network, they remain contained within small subgraphs (communities) at shorter times and then spill over onto larger communities at longer times. This definition of communities (and partitions) in terms of random walks makes the MS framework generally applicable to a wide range of network topologies, including directed networks, in contrast to standard hierarchical community detection algorithms [37–39]. MS uses an optimization to identify graph communities in which the flow of random walkers is contained over extended periods, uncovering a sequence of robust graph partitions of increasing coarseness (regulated by the Markov scale s). In the context of our mobility network, this set of partitions captures intrinsic scales of human mobility present in the data. See [25–28,40,41] and §4.2 for details of the methodology.

Figure 1*b* summarizes the MS analysis for our network, which was carried out with the `PyGenStability` Python package [42]. We find nine robust MS partitions $H(s_i)$ at different levels of resolution ($s_1, \ldots, s_9$) from fine to coarse, which comprise flow communities at different scales of human mobility (see electronic supplementary material, table S1 and figure S4 for further statistics and visualizations). Figure 1*c* shows that these data-driven flow communities correspond to geographic areas, even though our data only contain relational mobility flows without explicit geographic information. Furthermore, the nine partitions have a strong quasi-hierarchical structure, which is not imposed *a priori* by our graph partitioning method (see electronic supplementary material, figures S4 and S5). The obtained partitions thus reflect an inherent multiscale structure in the patterns of UK human mobility.

2.3. Comparing the intrinsic mobility scales at baseline with administrative nomenclature of territorial units for statistics regions

Next, we compare the MS partitions with NUTS regions, administrative and geographic regions defined at three hierarchical levels: NUTS1 build upon NUTS2 in turn consisting of NUTS3 regions. In the UK, the 174 NUTS3 regions represent counties and groups of unitary authorities; the 40 NUTS2 regions are groups of counties; and the 12 NUTS1 regions correspond to England regions, plus Scotland, Wales and Northern Ireland as whole nations (see electronic supplementary material, table S2 for further statistics). Our baseline data cover 170 NUTS3 regions, where the missing four are sparsely populated regions in the Scottish Highlands and Islands. The NUTS regions serve as a standard reference point for policy-making, and served to inform regionalized responses to COVID-19 in England (e.g. lockdowns in the North of England were applied to local authorities that form the NUTS2 region of Greater Manchester,

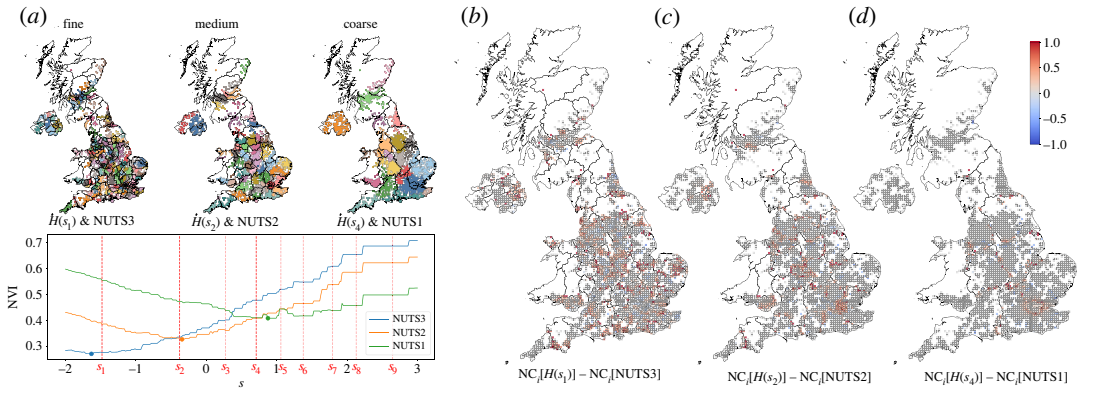

Figure 2. A posteriori comparison between MS partitions and NUTS regions. (*a*) The MS partitions across all scales are compared with the three levels of administrative NUTS regions: NUTS3 (fine), NUTS2 (medium) and NUTS1 (coarse). As indicated by the minima of the NVI, the NUTS3 division is closely similar to $H(s_1)$; NUTS2 to $H(s_2)$ and NUTS3 to $H(s_4)$. The maps show NUTS regions (lines) and MS partitions (coloured communities) for fine, medium and coarse levels. (*b–d*) The MS partitions display improved average nodal containment (NC) relative to NUTS regions (table 1), and the node measure NC_i (equation (4.6)) shows the regional improvements where administrative divisions do not conform naturally to mobility patterns. Fine scale: $H(s_1)$ captures boundary areas fragmented under NUTS3 (e.g. Cornwall–Devon boundary, North Wales, among many others). Medium scale: $H(s_2)$ captures densely connected areas in Central and East London, fragmented under NUTS2, as well as the commuter belt in Birmingham. Coarse scale: $H(s_4)$ naturally captures Greater London's commuter belt that is excluded from the London NUTS1 region.

Lancashire and West Yorkshire [43]). Comparing the data-driven MS partitions with NUTS regions is thus meant to explore to what degree administrative regions capture the patterns of mobility at the different scales and potential mismatches thereof.

In figure 2, we use the normalized variation of information (NVI; equation (4.3)) to evaluate the similarity of each of the three NUTS levels to the MS partitions at all scales. The best match of each NUTS level (as given by the minimum of NVI) is close to one of the robust partitions: NUTS3 corresponds closely to $H(s_1)$; NUTS2 to $H(s_2)$ and NUTS1 to $H(s_4)$. Hence, these three MS partitions of the mobility network capture the fine, medium and coarse scales in the UK, yet with some significant deviations from the administrative NUTS divisions. For instance, Greater London is separated from the rest of the South East at the level of NUTS1 regions, whereas the whole South East of England forms one flow community in partition $H(s_4)$. Similarly, the south of Wales is connected strongly via flows to the South West of England in partition $H(s_4)$, which is not reflected in the NUTS1 regions. On the other hand, the correspondence between NUTS3 regions and the fine MS partition $H(s_1)$ is strongest (lower value of NVI), with fewer such discrepancies between administrative and flow communities.

To evaluate further how the MS partitions capture the patterns of mobility, we compute two measures: the coverage $\mathcal{C}$ (equation (4.5)) (i.e. the ratio of mobility that remains within communities relative to the total mobility) and the average nodal containment NC (equation (4.7)) (i.e. the ratio of the outflow from each node that remains within its community relative to the total outflow from that node, then averaged over all nodes). High values of these measures (normalized between 0 and 100%) indicate that mobility flows are captured within the boundaries of the communities of the partition.

Table 1 shows that MS partitions are substantially better at reflecting baseline mobility than NUTS divisions since they have higher values for both average $\mathcal{C}$ and NC measures at all scales and especially at the finer scales. We have also evaluated both measures at a local level. Electronic supplementary material, figure S6*a* shows that the median of the coverage of individual communities $\mathcal{C}_k$ (equation (4.4)) is significantly higher for MS partitions (as compared with NUTS) for the fine and medium scales ($p < 0.0001$, Mann–Whitney). Electronic supplementary material, figure S6*b* shows that the median of the nodal containment of individual nodes NC_i (equation (4.6)) is also significantly higher for MS partitions relative to NUTS regions at fine, medium and coarse levels ($p < 0.001$, Mann–Whitney). Indeed, the maps in figure 2*b–d* show that $NC_i(MS) > NC_i(NUTS)$ in regions where the administrative NUTS boundaries cut through conurbations or closely connected towns or cities. A prominent example is Greater London, where the NUTS2 regions split areas in Central and East London that are tightly linked and thus captured better by the medium MS partition $H(s_2)$, and, similarly, the NUTS1 region of Greater London does not include its wider commuter belt that is

Table 1. Containment of baseline mobility flows within MS partitions compared with corresponding NUTS regions. MS partitions capture better the mobility patterns, as shown by higher values for both the average coverage $\mathcal{C}$ (equation (4.5)) and the average nodal containment NC (equation (4.7)).

		fine scale $H(s_1)$/NUTS3	middle scale $H(s_2)$/NUTS2	coarse scale $H(s_4)$/NUTS1
$\mathcal{C}$ (%)	MS	92.1	98.4	99.7
	NUTS	90.1	95.2	98.9
NC (%)	MS	86.6	95.5	98.1
	NUTS	72.8	88.3	95.8

naturally captured by the coarse MS partition $H(s_4)$. Similar commuter belt effects are observed, e.g. on the medium level for Birmingham, and on the fine level for Plymouth, which has associated flows across the Cornwall–Devon boundary.

2.4. Comparing the fine mobility scale at baseline with labour-related travel to work areas

We next compare the MS partitions with TTWAs, a different geography that divides the UK into 228 local labour markets computed from 2011 Census data recording place of residency and place of work [29]. Our baseline network has mobility data for 197 of the 228 TTWAs, with missing areas in rural areas of Scotland, Wales and the North of England (see figure 3*a* and further statistics in electronic supplementary material, table S3).

The TTWAs are intended to reflect local labour markets, and the ensuing commuting between home and place of work, and are thus expected to be linked to small scales. Indeed, as measured by the NVI, the TTWA division is most similar to the NUTS3 level of all NUTS divisions (see electronic supplementary material) and, consistently, most similar to the fine-scale MS partition, $H(s_1)$. Reassuringly, $H(s_1)$ is more similar to TTWA than to NUTS3, since both the TTWA division and our MS partitions are data driven with a basis in mobility patterns. Yet, there are local discrepancies, e.g. $H(s_1)$ combines multiple TTWAs into a single cluster in Cornwall or Northern Ireland, whereas the single TTWA in Greater London corresponds to several smaller communities in $H(s_1)$ (figure 3*a*).

As mentioned earlier, we evaluate how the TTWA division captures the patterns of mobility. We find that the coverage $\mathcal{C}(\text{TTWA}) = 95.9\%$ is higher than for both NUTS3 and $H(s_1)$ (table 1), but the median of the coverage of individual communities $\mathcal{C}_k$, a local measure of coverage, is not significantly higher for the TTWAs relatively to $H(s_1)$ (figure 3*b*). Furthermore, the average nodal containment $\text{NC}(\text{TTWA}) = 81.3\%$ is lower than $H(s_1)$ (table 1), and its local version shows that the median of the nodal containment of individual nodes NC_i is significantly lower for TTWA ($p < 0.0001$, Mann–Whitney, figure 3*c*). Hence, the fine MS partition $H(s_1)$ captures better the mobility patterns in our baseline data than the TTWA division. This can be explained by potential changes in commuting patterns since the 2011 Census data on which the TTWAs are based, and by the fact that Facebook mobility data also includes trips for leisure, commercial and other activities beyond commuting to work.

2.5. The contraction of the UK mobility under lockdown and its relation to the baseline mobility multiscale network

The first nationwide COVID-19 lockdown in the UK was imposed on 24 March 2020, instructing the British public to stay at home except for limited purposes. Over the following months, restrictions were gradually eased to allow pupils to return to school (1 June 2020 in England but 17 August 2020 in Scotland), businesses to reopen (non-essential shops reopened on 13 June 2020 in England but 13 July in Scotland) and people to travel more freely for leisure purposes (13 May 2020 in England but 8 July 2020 in Scotland) [44]. We have analysed the response to these restrictions using the time-dependent Facebook Movement maps [24] from 10 March to 18 July 2020 (131 days or 18 weeks). We construct mobility networks for each day, $G(d)$, and week, $G(w)$, defined on the same nodes (i.e. tiles) as the baseline network G (see §4.1).

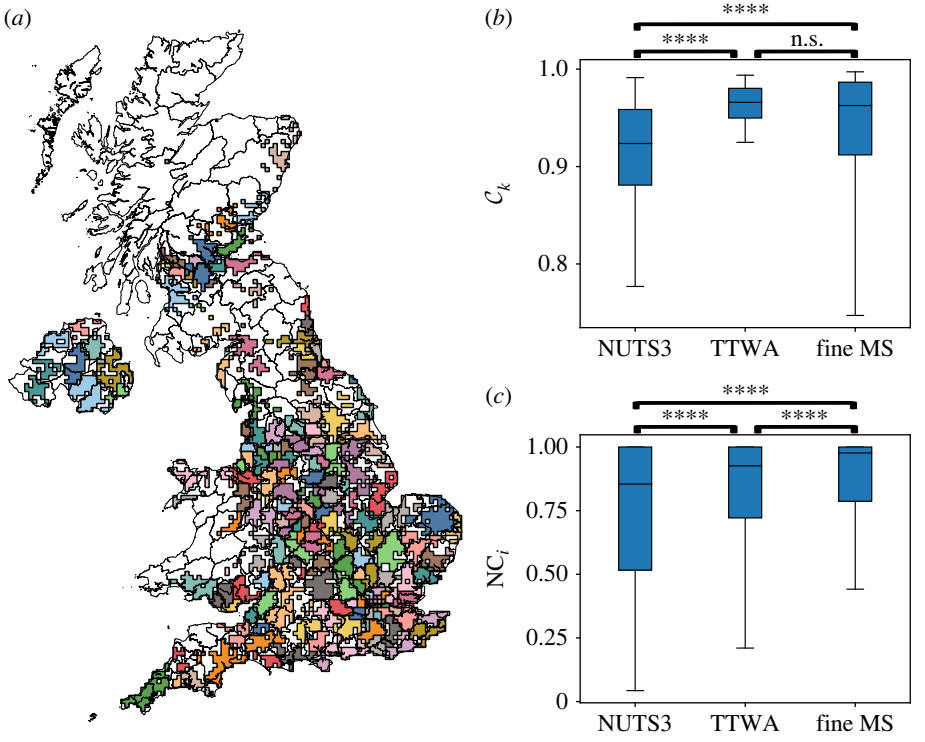

Figure 3. *A posteriori* comparison between the fine MS partition and TTWAs. (*a*) The fine-scale MS partition $H(s_1)$ is most similar to the division into TTWAs (electronic supplementary material, figure S7) as shown by the overlayed map, where lines separate TTWAs and MS communities (fine scale) are indicated by different colours. Although well aligned, there are some discrepancies, e.g. $H(s_1)$ combines multiple TTWAs into a single community in Cornwall or Northern Ireland. (*b*,*c*) The flow coverage of fine MS partition is compared with NUTS3 and TTWAs: (*b*) community coverage (equation (4.4)) and (*c*) nodal containment (equation (4.6)). Both fine MS and TTWA have significantly higher coverage than NUTS3, and fine MS has significantly higher nodal containment than both NUTS3 and TTWA. Statistical significance was determined using the Mann–Whitney test (**** indicates $p < 0.0001$ and n.s. indicates $p > 0.05$).

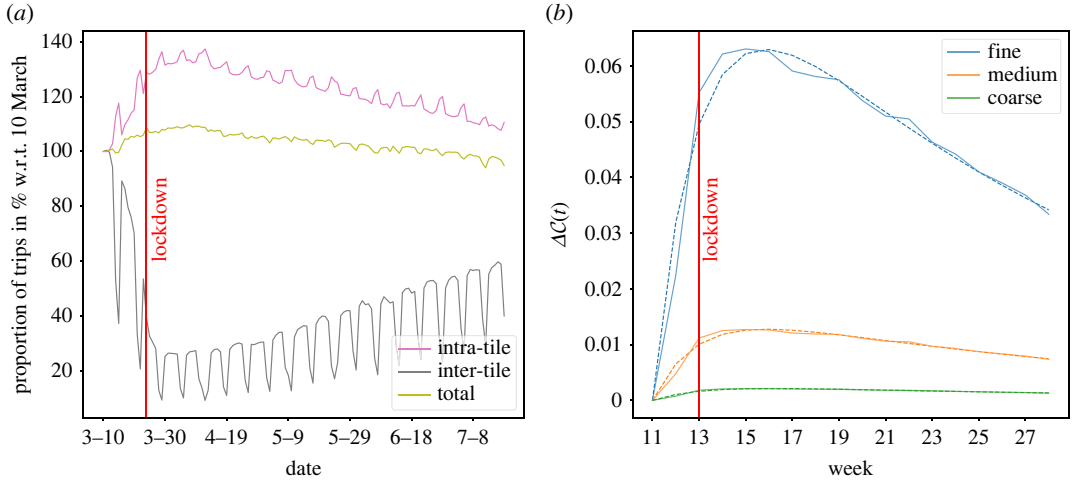

Figure 4. Temporal response of mobility networks to lockdown restrictions. The vertical red lines mark the official start of the first lockdown in the UK (24 March 2020). (*a*) Proportion (in %) of the number of daily trips (intra-tile, inter-tile, total) with respect to 10 March 2020. (*b*) Relative change of coverage $\Delta\mathcal{C}$ of MS partitions (fine, medium and coarse scales) measured with respect to the first week of the study period (Week 11). $\Delta\mathcal{C}$ improves for all scales, especially for the finer scales. Solid lines correspond to the observed values; dashed lines are fits of the activation response function (equation (2.4)).

Figure 4*a* shows the temporal change of the number of trips (intra-tile, inter-tile and total) relative to 10 March 2020, the first day of our study period. It is interesting to note that the decrease in mobility was already taking hold rapidly from 10 March, two weeks before the official enforcement of the lockdown.

Table 2. Parameters of temporal response of $\Delta\mathcal{C}(t)$ for the MS partitions. Estimated values and 95% confidence intervals for the amplitude α and characteristic time $1/\lambda$ of the external stimulus, and the characteristic recovery time $1/\beta$ towards pre-stimulus values obtained from fitting the activation response function (2.4) to the coverage values of the fine, medium and coarse MS partitions (figure 4*b*). Electronic supplementary material, table S4 provides all fitting parameters for all nine MS partitions.

	α (95% CI)	$1/\beta$ (95% CI)	$1/\lambda$ (95% CI)
Fine scale	0.042 (0.036–0.050)	16.4 (12.5–21.5)	2.0 (1.6–2.7)
Medium scale	0.0086 (0.0074–0.0101)	18.8 (14.6–24.3)	1.9 (1.5–2.5)
Coarse scale	0.0014 (0.0012–0.0016)	20.9 (15.7–28.0)	2.0 (1.6–2.6)

We find that whilst the total number of trips remained largely unchanged throughout the period, the number of inter-tile trips decreased sharply to approximately 25% of the initial value, followed by a steady increase towards levels of approximately 50% at the end of the study period in mid-July 2020. Conversely, the number of intra-tile trips increased to a maximum of 130% after lockdown before decreasing steadily to approximately 105% by mid-July 2020. Therefore, lockdown induced a redistribution from inter-tile to intra-tile trips as a result of a reduction in commuting and long-distance travel, with mobility reverting to local neighbourhoods.

The observed contraction of human mobility towards local neighbourhoods is consistent with the multiscale structure that was already present in the baseline mobility network pre-lockdown. The coverage $\mathcal{C}$ of all MS partitions increased over lockdown, with larger relative improvement for the finer scales (figure 4*b* and electronic supplementary material, figure F8). The surge in coverage induced by lockdown, which then decays towards its pre-lockdown value, can be modelled with a simple linear model under an external stimulus $\alpha e^{-\lambda t}$. The relative change from the initial value is then given by [45],

$$\Delta\mathcal{C}(t) := \frac{\mathcal{C}(t) - \mathcal{C}(t_0)}{\mathcal{C}(t_0)} = \frac{\alpha}{\beta - \lambda}(\mathrm{e}^{-\lambda t} - \mathrm{e}^{-\beta t}), \tag{2.4}$$

from which we estimate the amplitude (α) and characteristic time ($1/\lambda$) of the external stimulus, as well as the characteristic recovery time ($1/\beta$) of the system towards its pre-stimulus value (see §4 for details). Figure 4*b* shows the fits of $\Delta\mathcal{C}(t)$ (dashed lines) with estimated parameters in table 2. The fine MS partition exhibits the largest relative increase $\Delta\mathcal{C}(t)$ peaking at approximately 6%. The medium and coarse partitions peak at approximately 1 and 0.1%, respectively. This is also captured by the values of α and indicates that during lockdown people reverted to local mobility neighbourhoods already present in pre-lockdown patterns. The adaptation to the new COVID-19 situation and the pre-announcement of lockdown occurs quickly (over a characteristic time of $1/\lambda \sim 2$ weeks), signifying that adoption was fast and was already in progress before the official start date of lockdown. Mobility patterns then returned towards pre-lockdown values over longer time scales $1/\beta$ between 16.4 weeks (fine scale) and 20.9 weeks (coarse scale) reflecting a slow re-adaptation following the new situation and loosening of restrictions.

To highlight the local differences in the temporal response to the lockdown, figure 5 shows the parameters of the temporal fits for the community coverages $\Delta\mathcal{C}_k$ for all the communities in the fine-scale MS partition. We observe that urban centres like London, Birmingham, Liverpool or Manchester experience the strongest changes in the fine-scale coverage (high values of α) yet with faster recovery times (low values of $1/\beta$). Conversely, rural areas, which were already more constrained to local communities pre-lockdown, exhibit smaller but long-lived effects in the coverage at the local level. Our method also captures divergent trends across the different nations of the UK. For example, Scottish regions show longer time scales of recovery than most regions in England, consistent with the fact that Scotland maintained more stringent lockdown restrictions for a longer time [44], e.g. domestic travel restrictions were eliminated in Scotland only on 8 July 2020 and schools reopened on 17 August 2020, in contrast to 13 May and 1 June 2020 in England, respectively.

3. Discussion

Taking advantage of recent data availability, we have studied here the intrinsic multiscale structure of human mobility using, as a motivating example, UK data collected before and during the first COVID-19 lockdown. Firstly, we generated a directed mobility graph from geospatial Facebook

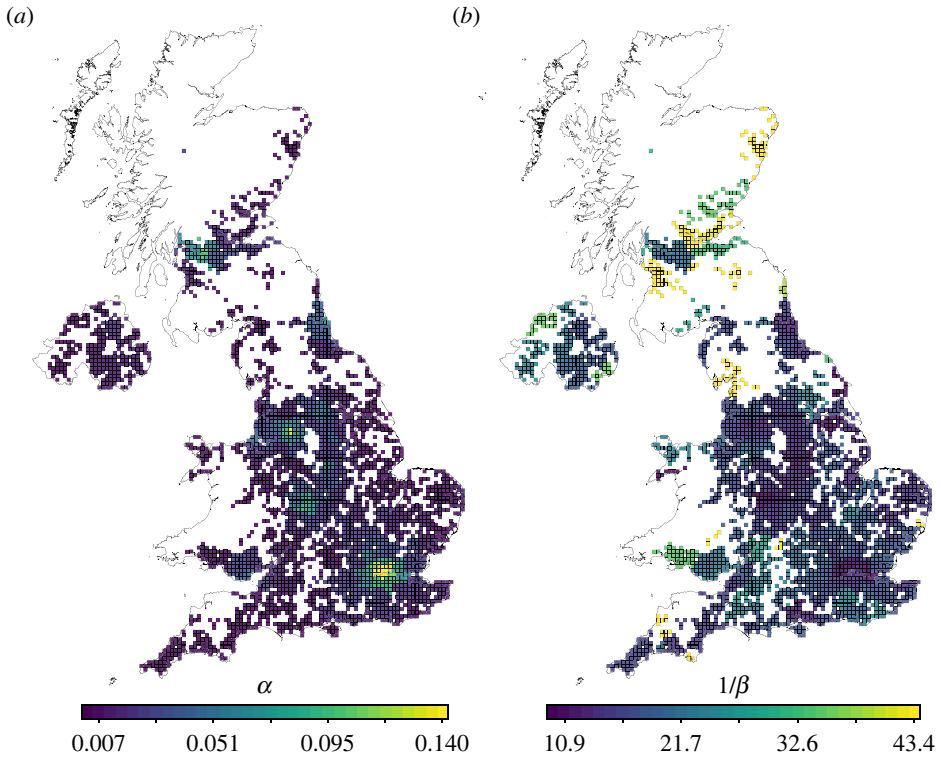

Figure 5. Regional differences in the temporal response to the lockdown. The maps show the fitting parameters of the activation response function for the weekly coverage $\mathcal{C}_k$ of the communities in the finest MS partition. (*a*) The shock amplitude α is high for urban centres (most notably London, Birmingham, Manchester and Glasgow) and low for rural areas. (*b*) The time scale of recovery $1/\beta$ is low for urban centres but high for rural areas, especially in Cornwall, Scotland or the Morecambe Bay area in North West England. Scotland shows longer recovery times due to different calendars for the lifting of restrictions relative to the rest of the UK.

Movement maps collected before lockdown, and exploited multiscale graph clustering (MS) to identify inherent flow communities at different levels of resolution (or scales) in the baseline data in an unsupervised manner. Three of the MS partitions so identified are of similar granularity to the NUTS hierarchy, yet with improved mobility coverage and nodal containment, also revealing areas of mismatch between human mobility and administrative divisions. Furthermore, we find that the fine MS partition, which captures local mobility in our data, shows high similarity to the division into TTWAs obtained from census residency and work location data to characterize local labour markets.

We then analysed spatiotemporal mobility data collected during the first UK COVID-19 lockdown. We found increased mobility coverage for MS partitions, especially at the fine scale, suggesting that the mobility contraction during this natural experiment reverted to scales already present in the pre-lockdown data. Indeed, given that our MS communities are found through a random walk on a graph weighted by pre-lockdown trip frequency of natural mobility, the fine scales capture frequent trips that were not suppressed during lockdown, whereas the coarse scales are associated with less frequent trips over longer geographic distances for leisure or business.

The enhancement of coverage induced by lockdown is well captured by a linear decay model, whose parameters allow us to quantify regional differences, including differing trends across urban and rural areas and across the UK nations consistent with distinct lockdown regulations.

In this study, we have identified intrinsic communities at different scales extracted from a static network (our pre-lockdown baseline) and then studied how changes in mobility over the early months of the pandemic evolved relative to those inherent communities. The aim was to test the relevance of the inherent scales under this natural experiment by quantifying the extent to which mobility patterns conformed to communities derived from the baseline configuration. A complementary approach would be to instead obtain communities through additional analysis of the sequence of daily (or weekly) mobility networks using temporal community detection, e.g. via the recently proposed flow stability [46], an extension of MS to temporal networks. This would be an interesting direction for future research.

Our study has several limitations. Whilst the 'Facebook Movement map' data is aggregated from 16 million UK Facebook users who enable location sharing (over 20% of the total UK population), the

observed sample might be biased and not representative of the general UK population [30]. Furthermore, inter-tile flows with fewer than 10 trips within an 8 h period are suppressed to prevent individual identification. In densely populated areas, our observed mobility data are thus more likely to be representative of human mobility, whereas this assumption is less likely to hold in rural areas, a limitation that can have an effect on comparisons with NUTS regions and TTWAs. However, such low-frequency connections account for a comparatively small number of the total trips and are not expected to affect the obtained MS partitions. This study also assumes rates of utilization and activation of location sharing within the Facebook app remain constant, yet this limitation is mitigated by the derivation of flow partitions from average baseline data, rather than post-pandemic mobility information.

Our work contributes to the current interest in the study of intrinsic scales in human mobility [22]. A recent study identified 'spatial containers' from granular GPS traces [6] organized in a nested hierarchy specific to each individual. Similarly, we also reveal a multiscale organization of human mobility, but instead obtain a data-driven, unsupervised quasi-hierarchical community structure at the population level. Because our MS community detection is based on a diffusion on a mobility graph, the flow communities at different scales provide insights into the importance of physical and political geographies, and reveal the scales at which lockdown introduced frictions by restricting natural mobility.

4. Methods

4.1. Mobility data and network construction

4.1.1. Data

Facebook Movement maps [24,30] provide movement data between geographic tiles as codified by the *Bing Maps Tile System* [47]. For the UK, there are 5436 geographic tiles with widths between 4.8 and 6.1 km (see electronic supplementary material, figure S1*a*). For users that enable location sharing, Facebook computes the dominant tiles, in which the user spends the most time over adjacent 8 h time windows. The 'trips' correspond to movements between dominant tiles across adjacent time windows. The dataset then provides the number of trips within each tile and to any other tile at intervals of 8 h for all users. The data are anonymized by Facebook prior to release using proprietary aggregation methods, including the addition of small amounts of random noise, spatial smoothing and dropping counts of less than 10 trips within an 8 h period to avoid identifiability. Our data further aggregate the three 8 h datasets for a given day. The data used in this study are the most comprehensive publicly available mobility dataset providing origin–destination data over time and covering the period of the COVID-19 pandemic. To our knowledge, no other dataset was available in the UK with better spatial and temporal resolution.

4.1.2. Network construction

Given a directed graph G, a weakly connected component (WCC) is a subgraph where each pair of nodes in the WCC is connected by an *undirected* path. Similarly, in a strongly connected component (SCC), each pair of nodes is connected by a *directed* path [48]. The largest WCC is denoted as LWCC and the largest strongly connected component as LSCC.

As a baseline, we use pre-lockdown data consisting of mobility flows averaged over the 45 days before 10 March 2020. To obtain the baseline network G, we remove the self-loops (i.e. we do not include intra-tile trips) and we *define* G as the LSCC of the graph of flows. As shown in electronic supplementary material, figure S1, the LWCC and LSCC are similar and 98.8% of the WCCs are singletons, and hence, the LSCC captures the large majority of relevant flows while simplifying the mathematical interpretation of the results.

We also use time series of mobility flows from 10 March to 18 July 2020 inclusive (131 days or 18 weeks) to build daily mobility networks $G(d)$, $d = 1, \ldots, 131$ and weekly mobility networks $G(w)$, $w = 1, \ldots, 18$ (by averaging the daily networks over calendar weeks). In all cases, the networks are defined on the same set of nodes as G, and we remove self-loops as earlier.

4.2. Multiscale community detection with Markov stability analysis

Here, we provide a brief outline of the MS framework. For a fuller description, see the electronic supplementary material and in-depth treatments, including extensions to other types of graph processes, in references [25–27,40].

Consider a weighted and directed graph G with adjacency matrix A. Let $L = I - D_{\text{out}}^{+}A$ denote the *random walk Laplacian* matrix, where I is the identity matrix, and D_{out}^{+} denotes the pseudo-inverse of the diagonal out-degree matrix. The matrix L defines a continuous-time Markov process on G governed by the diffusive dynamics

$$\frac{\mathrm{d}\mathbf{p}}{\mathrm{d}r} = -\mathbf{p}L, \tag{4.1}$$

where $\mathbf{p}(r)$ is a $1 \times N$ node vector of probabilities, and r is the Markov scale. The solution to this equation is given by $\mathbf{p}(r) = \mathbf{p}(0)\exp(-Lr)$, and the matrix exponential defines transition probabilities of the Markov process (see electronic supplementary material). This process converges to a stationary distribution $\boldsymbol{\pi}$ given by $\boldsymbol{\pi}L = 0$.

The goal of MS is to obtain partitions of the graph into $c(r)$ communities such that the probability flow described by (4.1) is optimally contained within the communities as a function of r. MS solves this problem by maximizing the following function:

$$H(r) = \arg\max_{H} \operatorname{Tr}[H^{T}(\boldsymbol{\Pi}\exp(-Lr) - \boldsymbol{\pi}^{T}\boldsymbol{\pi})H], \tag{4.2}$$

where $\boldsymbol{\Pi} = \operatorname{diag}(\boldsymbol{\pi})$, and the matrix $H(r)$ is a $N \times c(r)$ partition indicator matrix with $H(r)_{ij} = 1$ if i is part of community j, and 0 otherwise. We thus obtain a series of optimized partitions over the Markov scales described by the matrices $H(r)$. The scales are more naturally described in log scale, so we *redefine* the Markov scale as $s = \log_{10}(r)$. The optimization (4.2) is carried out using the Louvain algorithm [49] through the implementation in the `PyGenStability` python package [42].

4.2.1. Comparing partitions with the normalized variation of information

To assess the quality of the partitions, we use the NVI as a similarity measure for partitions [50,51]. Consider two partitions described by $H(s)$ and $H(s')$ with potentially different numbers of communities. The NVI is defined as follows:

$$0 \leq \mathrm{NVI}(s, s') := \frac{\mathrm{VI}(s, s')}{\mathcal{H}(s, s')} \leq 1, \tag{4.3}$$

where $\mathrm{VI}(s, s')$ is the variation of information [52] and $\mathcal{H}(s, s')$ is the mutual information between $H(s)$ and $H(s')$. The NVI is a metric, and low values indicate a high similarity between the partitions [51]. Using NVI has the advantage of being a universal similarity metric [53], i.e. if $H(s)$ and $H(s')$ are similar under any non-trivial metric, then they are also similar under NVI [51].

4.2.2. Scale selection algorithm

After obtaining optimized partitions $H(s)$ for a sequence of m Markov scales $S = \{s_1, s_2, \ldots, s_m\}$, we select partitions that describe the network structure robustly at different levels of resolution. Robust partitions are persistent across scales and reproducible under the non-convex Louvain optimization for its particular scale [27]. We formalize these requirements using NVI as follows: (i) the persistence across scales is assessed by computing the pairwise NVI for partitions across different scales s and s' leading to a $m \times m$ symmetric matrix denoted by $\mathrm{NVI}(s, s')$, where regions of low values indicate high persistence across scales; (ii) for each Markov scale s, the robustness is evaluated by repeating the Louvain optimization (300 times in our study) with different random initialization and computing the average pairwise NVI for the resulting ensemble of partitions, denoted by $\mathrm{NVI}(s)$, such that low values indicate strong reproducibility of the optimization.

As an aid to scale selection, we propose here an algorithm that processes the information contained in $\mathrm{NVI}(s, s')$ and $\mathrm{NVI}(s)$ sequentially. First, we use tools from image processing to evaluate the block structure of the $\mathrm{NVI}(s, s')$ matrix and apply average pooling [54] with a kernel of size k (and padding) such that the pooled diagonal $\widehat{\mathrm{NVI}}(s)$ quantifies the average pairwise similarity of all partitions corresponding to scales in the neighbourhood $\mathcal{B}_k(s) = \{u \in S : 0 < |u - s| \leq k\}$ of scale s. We then compute the smoothed version of $\widehat{\mathrm{NVI}}(s)$, denoted Block $\mathrm{NVI}(s)$. Blocks of low values of $\mathrm{NVI}(s, s')$ correspond to basins around local minima of the Block $\mathrm{NVI}(s)$. We then obtain the minimum of $\mathrm{NVI}(s)$ for each basin and determine those as the robust scales of the network. Our scale selection algorithm is implemented in the `PyGenStability` package [42].

4.3. Measures of flow containment: coverage and nodal containment

Consider the adjacency matrix A of the mobility graph G and a $N \times c$ indicator matrix H for a partition of G into c communities. Let us also define $\tilde{A}$, the adjacency matrix of the graph with self-loops that contains the intra-tile flows on the diagonal. Then $F = H^T \tilde{A} H$ is the $c \times c$ lumped adjacency matrix where the element $(H^T \tilde{A} H)_{kl}$ corresponds to the mobility flow from community k to community l. The *coverage* of community k, $\mathcal{C}_k(H)$, is defined as follows:

$$0 \leq \mathcal{C}_k(H) := (\hat{D}^+ F)_{kk} \leq 1, \tag{4.4}$$

where $\hat{D}^+$ is the pseudo-inverse of $\hat{D} = \mathrm{diag}(\hat{\boldsymbol{d}})$, where $\hat{\boldsymbol{d}} = F\mathbf{1}_c$. $\mathcal{C}_k(H)$ can be interpreted as the probability of the lumped Markov process to remain in state k; hence, high values of $\mathcal{C}_k(H)$ indicate that community k covers well the flows emerging from the community.

The coverage of a partition $\mathcal{C}(H)$ is standard and is defined as the ratio of flows contained within communities by the total amount of flow [55]. It is easy to see that this is given by the weighted average

$$0 \leq \mathcal{C}(H) = \frac{\sum_k \hat{\boldsymbol{d}}_k \mathcal{C}_k(H)}{\sum_k \hat{\boldsymbol{d}}_k} \leq 1. \tag{4.5}$$

High values of $\mathcal{C}(H)$ indicate that mobility flows are contained well within the communities of the partition and movement across different communities is limited.

The *nodal containment* NC_i of node i quantifies the proportion of flow emerging from i that is contained within its community in a partition H,

$$0 \leq \mathrm{NC}_i(H) := \frac{(AH)_{iC_i}}{d_i} \leq 1, \tag{4.6}$$

where C_i is the community of node i and $d_i = (A\,\mathbf{1}_N)_i$. Large values of NC_i indicate that the mobility flows emerging from node i are largely contained within its assigned community, indicating a good node assignment. Hence, NC_i measures the containment of flows from a node-centred perspective.

To obtain a partition-level measure, we define the *average nodal containment* $\mathrm{NC}(H)$

$$0 \leq \mathrm{NC}(H) := \frac{1}{N} \sum_{i=1}^{N} \mathrm{NC}_i(H) \leq 1, \tag{4.7}$$

where N is the number of nodes.

4.4. Response to an exponentially decaying shock

The response of a variable $x(t)$ to a shock can be modelled as a linear ordinary differential equation under a stimulus $R(t)$,

$$\frac{\mathrm{d}x}{\mathrm{d}t} = -\beta x + R(t), \quad x(0) = 0, \tag{4.8}$$

where $1/\beta$ is the characteristic relaxation time of the system, and we assume here an exponentially decaying external stimulus $R(t) := \alpha\, \mathrm{e}^{-\lambda t}$, with amplitude $\alpha \geq 0$ and characteristic decay time $1/\lambda$. The solution of (4.8) is given by [45]

$$x(t) = \frac{\alpha}{\beta - \lambda} (\mathrm{e}^{-\lambda t} - \mathrm{e}^{-\beta t}).$$

We use the Levenberg–Marquardt algorithm [56] implemented in the LMFIT [57] python package to fit the activation response function $x(t)$ to a set of n data points $(\tilde{t}_i, \tilde{x}_i)$ by minimizing the sum of squares

$$\chi^2 := \sum_{i=1}^{n} (x(\tilde{t}_i) - \tilde{x}_i)^2 \tag{4.9}$$

to determine parameter estimates $\hat{\alpha}$, $\hat{\beta}$ and $\hat{\lambda}$. Confidence intervals are obtained from an F-test [58].

Ethics. This work did not require ethical approval from a human subject or animal welfare committee.

Data accessibility. Data used in this study were accessed through Facebook's 'Data for Good' program: https://dataforgood.facebook.com/dfg/tools/movement-maps. Shapefiles for the NUTS (2018) regions and TTWAs (2011) in the UK are available from the Open Geography Portal https://geoportal.statistics.gov.uk/ under the Open Government Licence v. 3.0 and contain OS data © Crown copyright and database right 2023. We host data of the UK mobility networks alongside code to reproduce all results and figures in our study on GitHub: https://github.

com/barahona-research-group/MultiscaleMobilityPatterns. A copy of this code has been archived to the Zenodo repository: https://doi.org/10.5281/zenodo.8362989 [59].

Electronic supplementary material is available online [60].

Declaration of AI use. We have not used AI-assisted technologies in creating this article.

Authors' contributions. D.J.S.: conceptualization, formal analysis, investigation, methodology, software, validation, visualization, writing—original draft and writing—review and editing; J.C.: conceptualization, data curation, formal analysis, supervision and writing—review and editing; M.B.: conceptualization, methodology, supervision and writing—review and editing.

All authors gave final approval for publication and agreed to be held accountable for the work performed therein.

Conflict of interest declaration. We declare we have no competing interests.

Funding. M.B. and J.C. acknowledge support from EPSRC grant no. EP/N014529/1 supporting the EPSRC Centre for Mathematics of Precision Healthcare. J.C. acknowledges support from the Wellcome Trust (215938/Z/19/Z). D.J.S. acknowledges support from the EPSRC (PhD studentship through the Department of Mathematics at Imperial College London).

Acknowledgements. We thank Robert Peach and Michael Schaub for valuable discussions. We also thank Alex Pompe for insights regarding data collection. Finally, we thank our anonymous reviewers for their constructive feedback and helpful suggestions.

References

1. Sim A, Yaliraki SN, Barahona M, Stumpf MPH. 2015 Great cities look small. *J. R. Soc. Interface* **12**, 1–9. (doi:10.1098/rsif.2015.0315)
2. Xu F, Li Y, Jin D, Lu J, Song C. 2021 Emergence of urban growth patterns from human mobility behavior. *Nat. Comput. Sci.* **1**, 791–800. (doi:10.1038/s43588-021-00160-6)
3. Wang Q, Taylor JE. 2016 Patterns and limitations of urban human mobility resilience under the influence of multiple types of natural disaster. *PLoS ONE* **11**, e0147299. (doi:10.1371/journal.pone.0147299)
4. Brockmann D, Helbing D. 2013 The hidden geometry of complex, network-driven contagion phenomena. *Science* **342**, 1337–1342. (doi:10.1126/science.1245200)
5. Sobolevsky S, Szell M, Campari R, Couronné T, Smoreda Z, Ratti C. 2013 Delineating geographical regions with networks of human interactions in an extensive set of countries. *PLoS ONE* **8**, e81707. (doi:10.1371/journal.pone.0081707)
6. Alessandretti L, Aslak U, Lehmann S. 2020 The scales of human mobility. *Nature* **587**, 402–407. (doi:10.1038/s41586-020-2909-1)
7. González MC, Hidalgo CA, Barabási AL. 2008 Understanding individual human mobility patterns. *Nature* **453**, 779–782. (doi:10.1038/nature06958)
8. Song C, Koren T, Wang P, Barabási AL. 2010 Modelling the scaling properties of human mobility. *Nat. Phys.* **6**, 818–823. (doi:10.1038/nphys1760)
9. Simini F, González MC, Maritan A, Barabási AL. 2012 A universal model for mobility and migration patterns. *Nature* **484**, 96–100. (doi:10.1038/nature10856)
10. Hale T *et al.* 2021 A global panel database of pandemic policies (Oxford COVID-19 Government Response Tracker). *Nat. Hum. Behav.* **5**, 529–538. (doi:10.1038/s41562-021-01079-8).
11. Buckee CO *et al.* 2020 Aggregated mobility data could help fight COVID-19. *Science* **368**, 145.2–146. (doi:10.1126/science.abb8021)
12. Chang S et al. 2021 Mobility network models of COVID-19 explain inequities and inform reopening. *Nature* **589**, 82–87. (doi:10.1038/s41586-020-2923-3).
13. Herren CM *et al.* 2020 Democracy and mobility: a preliminary analysis of global adherence to non-pharmaceutical interventions for COVID-19. *SSRN Journal*. (doi:10.2139/ssrn.3570206).
14. Cintia P *et al.* 2020 The relationship between human mobility and viral transmissibility during the COVID-19 epidemics in Italy. *arXiv preprint*. (doi:10.48550/arXiv.2006.03141)
15. Oliver N *et al.* 2020 Mobile phone data for informing public health actions across the COVID-19 pandemic life cycle. *Sci. Adv.* **6**, abc0764. (doi:10.1126/sciadv.abc0764)
16. Unwin HJT *et al.* 2020 State-level tracking of COVID-19 in the United States. *Nat. Commun.* **11**, 6189. (doi:10.1038/s41467-020-19652-6)
17. Nouvellet P *et al.* 2021 Reduction in mobility and COVID-19 transmission. *Nat. Commun.* **12**, 1090. (doi:10.1038/s41467-021-21358-2)
18. Galeazzi A, Cinelli M, Bonaccorsi G, Pierri F, Schmidt AL, Scala A, Pammolli F, Quattrociocchi W. 2021 Human mobility in response to COVID-19 in France, Italy and UK. *Sci. Rep.* **11**, 13141. (doi:10.1038/s41598-021-92399-2)
19. Bonaccorsi G *et al.* 2020 Economic and social consequences of human mobility restrictions under COVID-19. *Proc. Natl Acad. Sci. USA* **117**, 15 530–15 535. (doi:10.1073/pnas.2007658117)
20. Bonaccorsi G, Pierri F, Scotti F, Flori A, Manaresi F, Ceri S, Pammolli F. 2021 Socioeconomic differences and persistent segregation of italian territories during COVID-19 pandemic. *Sci. Rep.* **11**, 21174. (doi:10.1038/s41598-021-99548-7)
21. Møllgaard PE, Lehmann S, Alessandretti L. 2022 Understanding components of mobility during the COVID-19 pandemic. *Phil. Trans. R. Soc. A* **380**, 20210118. (doi:10.1098/rsta.2021.0118)
22. Arcaute E. 2020 Hierarchies defined through human mobility. *Nature* **587**, 372–373. (doi:10.1038/d41586-020-03197-1)
23. Brockmann D, Hufnagel L, Geisel T. 2006 The scaling laws of human travel. *Nature* **439**, 462–465. (doi:10.1038/nature04292)
24. Facebook Data for Good. 2020 *Disease Prevention Maps*. See https://dataforgood.facebook.com.
25. Delvenne JC, Yaliraki SN, Barahona M. 2010 Stability of graph communities across time scales. *Proc. Natl Acad. Sci. USA* **107**, 12 755–12 760. (doi:10.1073/pnas.0903215107)
26. Delvenne JC, Schaub MT, Yaliraki SN, Barahona M. 2013 The stability of a graph partition: a dynamics-based framework for community detection. In *Dynamics on and of complex networks* (eds A Mukherjee, M Choudhury, F Peruani, N Ganguly, B Mitra), vol. 2, pp. 221–242. New York, NY: Springer New York. (doi:10.1007/978-1-4614-6729-8_11)
27. Lambiotte R, Delvenne JC, Barahona M. 2014 Random walks, Markov processes and the multiscale modular organization of complex networks. *IEEE Trans. Netw. Sci. Eng.* **1**, 76–90. (doi:10.1109/TNSE.2015.2391998)
28. Bacik KA, Schaub MT, Beguerisse-Díaz M, Billeh YN, Barahona M. 2016 Flow-based network analysis of the *Caenorhabditis elegans* connectome. *PLoS Comput. Biol.* **12**, e1005055. (doi:10.1371/journal.pcbi.1005055)
29. Office for National Statistics. 2016 *Travel to work area analysis in Great Britain: 2016*. See https://www.ons.gov.uk/employmentandlabourmarket/peopleinwork/employmentandemployeetypes/articles/traveltoworkareaanalysisingreatbritain/2016.
30. Maas P. 2019 Facebook disaster maps: aggregate insights for crisis response & recovery. In *Proc. of the 25th ACM SIGKDD Int. Conf. on Knowledge Discovery & Data Mining*, p. 3173. (doi:10.1145/3292500.3340412).
31. Beguerisse-Díaz M, Garduño-Hernández G, Vangelov B, Yaliraki SN, Barahona M. 2014 Interest communities and flow roles in directed networks: the Twitter network of the UK riots. *J. R. Soc. Interface* **11**, 20140940. (doi:10.1098/rsif.2014.0940)
32. Brin S, Page L. 1998 The anatomy of a large-scale hypertextual web search engine. *Comput.*

Netw. ISDN Syst. **30**, 107–117. (doi:10.1016/S0169-7552(98)00110-X)

33. Arnaudon A, Peach RL, Barahona M. 2020 Scale-dependent measure of network centrality from diffusion dynamics. *Phys. Rev. Res.* **2**, 033104. (doi:10.1103/PhysRevResearch.2.033104)
34. Levin DA, Peres Y, Wilmer EL. 2009 *Markov chains and mixing times*. Providence, RI: American Mathematical Society.
35. Perra N, Fortunato S. 2008 Spectral centrality measures in complex networks. *Phys. Rev. E* **78**, 036107. (doi:10.1103/PhysRevE.78.036107)
36. Schaub MT, Delvenne JC, Lambiotte R, Barahona M. 2019 Multiscale dynamical embeddings of complex networks. *Phys. Rev. E* **99**, 062308. (doi:10.1103/PhysRevE.99.062308)
37. Girvan M, Newman MEJ. 2002 Community structure in social and biological networks. *Proc. Natl Acad. Sci. USA* **99**, 7821–7826. (doi:10.1073/pnas.122653799)
38. Clauset A, Newman MEJ, Moore C. 2004 Finding community structure in very large networks. *Phys. Rev. E* **70**, 066111. (doi:10.1103/PhysRevE.70.066111)
39. Bonald T, Charpentier B, Galland A, Hollocou A. 2018 Hierarchical graph clustering using node pair sampling. *arXiv preprint*. (doi:10.48550/arXiv.1806.01664)
40. Lambiotte R, Delvenne JC, Barahona M. 2009 Laplacian dynamics and multiscale modular structure in networks. *arXiv preprint*. (doi:10.48550/arXiv.0812.1770)
41. Schaub MT, Delvenne JC, Yaliraki SN, Barahona M. 2012 Markov dynamics as a zooming lens for multiscale community detection: non clique-like communities and the field-of-view limit. *PLoS ONE* **7**, 0032210. (doi:10.1371/journal.pone.0032210)
42. Arnaudon A, Schindler DJ, Peach RL, Gosztolai A, Hodges M, Schaub MT, Barahona M. 2023 PyGenStability: multiscale community detection with generalized Markov stability. See https://github.com/barahona-research-group/PyGenStability. (doi:10.48550/ARXIV.2303.05385)
43. HM Government (UK). 2020 *The Health Protection (Coronavirus, Restrictions on Gatherings) (North of England) Regulations*. See https://www.legislation.gov.uk/uksi/2020/828/contents.
44. Grewal S, Wood A, Tatlow H, Hale T, Phillips T. 2021 *Variation in the response to COVID-19 across the four nations of the United Kingdom*. *BSG-WP-2020/035 Version 2.0*. Blavatnik School of Government. See https://www.bsg.ox.ac.uk/research/publications/variation-response-covid-19-across-four-nations-united-kingdom.
45. Beguerisse-Díaz M, Desikan R, Barahona M. 2016 Linear models of activation cascades: analytical solutions and coarse-graining of delayed signal transduction. *J. R. Soc. Interface* **13**, 1–10. (doi:10.1098/rsif.2016.0409)
46. Bovet A, Delvenne JC, Lambiotte R. 2022 Flow stability for dynamic community detection. *Sci. Adv.* **8**, eabj3063. (doi:10.1126/sciadv.abj3063)
47. Schwartz J. 2018 *Bing Maps Tile System*. See https://learn.microsoft.com/en-us/bingmaps/articles/bing-maps-tile-system.
48. Zweig KA. 2016 *Network analysis literacy: a practical approach to the analysis of networks*. Lecture Notes in Social Networks. Vienna, Austria: Springer.
49. Blondel VD, Guillaume JL, Lambiotte R, Lefebvre E. 2008 Fast unfolding of communities in large networks. *J. Stat. Mech: Theory Exp.* **2008**, P10008. (doi:10.1088/1742-5468/2008/10/p10008)
50. Vinh NX, Epps J, Bailey J. 2010 Information theoretic measures for clusterings comparison: variants, properties, normalization and correction for chance. *J. Mach. Learn. Res.* **11**, 2837–2854.
51. Kraskov A, Stögbauer H, Andrzejak RG, Grassberger P. 2003 Hierarchical clustering based on mutual information. *arXiv preprint*. (doi:10.48550/arXiv.q-bio/0311039)
52. Meilă M. 2003 Comparing clusterings by the variation of information. In *Learning theory and kernel machines*. Lecture notes in computer science (eds B Schölkopf, MK Warmuth), pp. 173–187. Berlin, Germany: Springer.
53. Li M, Chen X, Li X, Ma B, Vitanyi PMB. 2004 The similarity metric. *IEEE Trans. Inf. Theory* **50**, 3250–3264. (doi:10.1109/TIT.2004.838101)
54. Boureau YL, Ponce J, LeCun Y. 2010 A theoretical analysis of feature pooling in visual recognition. In *Proc. of the 27th Int. Conf. on Machine Learning, ICML'10*, pp. 111–118. Madison, WI: Omnipress.
55. Fortunato S. 2010 Community detection in graphs. *Phys. Rep.* **486**, 75–174. (doi:10.1016/j.physrep.2009.11.002)
56. Moré JJ. 1978 The Levenberg-Marquardt algorithm: implementation and theory. In *Numerical analysis*. Lecture Notes in Mathematics (ed. GA Watson), pp. 105–116. Berlin, Germany: Springer.
57. Newville M, Stensitzki T, Allen DB, Ingargiola A. 2014 LMFIT: non-linear least-square minimization and curve-fitting for Python. *Zenodo*. (doi:10.5281/zenodo.11813)
58. Vugrin KW, Swiler LP, Roberts RM, Stucky-Mack NJ, Sullivan SP. 2007 Confidence region estimation techniques for nonlinear regression in groundwater flow: three case studies. *Water Resour. Res.* **43**, 2005WR004804. (doi:10.1029/2005WR004804)
59. Schindler D. 2023 barahona-research-group/MultiscaleMobilityPatterns: Version 1.0.0. *Zenodo*. (doi:10.5281/zenodo.8362989)
60. Schindler DJ, Clarke J, Barahona M. 2023 Multiscale mobility patterns and the restriction of human movement. Figshare. (doi:10.6084/m9.figshare.c.6858353)